Supporting Information

Liu et al. 10.1073/pnas.1006611107

SI Text

S1. Modeling Parameters. The detailed parameters used in our model and the corresponding references are listed in Table S1.

S2. Fractional Binding Comparison with Experiment. The fractional binding ζ between the NC and the EC surface is described using the Langmuir binding model (11):

$$\zeta = \frac{C/K_d}{1 + C/K_d}, \qquad [S1]$$

where K_d is the calculated binding dissociation constant (equal to $1/K_a$) and C represents the NC concentration. In this model, the EC surface is discretized into multiple binding sites. Due to the polyvalent interactions between NC and EC, the discretization is performed by defining a minimal EC patch which can sustain complete NC binding. Such a patch is defined self-consistently through our MC simulations: in Fig. 2*B* in main manuscript and in Fig. S5 (right panels), the loci traced by the bound receptor-ligand pairs define such a minimal patch. According to the Langmuir model, the K_d is the binding dissociation constant defined with respect to this minimal EC surface patch. The fractional binding ζ is then defined as the fraction of minimal patches bound to NC relative to the saturation value. Fig. S1*A* shows the fractional binding curves generated from Eq. **S1**. The corresponding binding constants compare very favorably with experimental measurements, (Fig. S1*B*).

S3. Estimation of Rotational Volumes from Euler Angle Distributions. As described in (10), the rotational volumes in the bound state are estimated from the Euler angle fluctuations. Fig. S2 shows the distribution of the three Euler angles (ϕ, ψ and θ) in the equilibrium bound state: As shown in panels *A* and *B*, ϕ and ψ are distributed uniformly between 0 and 2π, however θ is peaked at a specific angle between 0 and π and follows a Gaussian distribution, see inset of panel *C*. The standard deviations of the three Euler angles are estimated from their distributions in Fig. S2, based on which the rotational volume $\Delta\omega$ in Eq. **9** in the main manuscript is calculated. Detailed formulation can also be found in ref. 10.

S4. Effect of NC Size. To test the effect of the NC size on binding, we investigate NC with diameter of 200 nm and antibody surface coverage of 74%. We observe an average of $5 \sim 6$ bonds although the system free energy decreases by about $4k_BT$ compared with 100 nm NC results of three bonds. In Fig. S3, we show the distribution of the reaction bond length d and ICAM-1 bending angle θ and compare with results for 100 nm NCs. Please refer to the main manuscript (Fig. 1) for the definitions of d and θ. As clearly shown in Fig. S3, more bonds with larger d and θ are formed with larger NC, indicating more weaker bonds compared with small NC although the number of bonds increase.

S5. Estimation of σ_s Where Multivalency Decreases from 2 to 1. As indicated in Fig. 3*A* in the main manuscript, we predict an exponential decay of binding affinity K_a as the antibody surface coverage σ_s drops below 100 Ab/NC (45%) because of the multivalency drop (from 3 to 2). We will expect another exponential decay of K_a when σ_s is so small that it is impossible to form the second bond. This occurs when the overlap of the NC and cell surface prevents bond formation as illustrated in Fig. S4. With the parameters listed in Table S1, the angle between two nearest bonds α may be calculated as $\alpha_0 = 123°$ when the NC overlaps the cell surface. For 100 nm NC with uniformly distributed antibodies, α is larger than α_0 when the number of antibodies is smaller than 4. Therefore, we estimate another exponential decay of binding affinity as $N_{ab} \lessapprox 4$ as a result of multivalency change from 2 to 1.

S6. PMF Profiles at Different Antibody Surface Coverages. Fig. S5 shows the PMF profiles and bond distributions for systems with different values of σ_s shown in Fig. 3*A* in the main manuscript.

S7. Multivalency vs. σ_s. Fig. S6 shows the effect of shear on the multivalency at different antibody surface coverages σ_s. The shear rate is $S = 6{,}000\ s^{-1}$, which corresponds to a shear stress of 6 Pa in water. As shown, the shear does impact the the multivalency at low surface coverage $\sigma_s \leq 14\%$ when the average multivalency $\lessapprox 2$, but has negligible effect at high antibody surface coverages when the average multivalency increases to 3.

S8. Biodistribution of NC in Other Organs. We have analyzed additional data on the biodistribution of anti-ICAM/particles shown in Fig. 3*B* of the main manuscript. These results, shown in Fig. S8 show that the uptake of the particles in the main reticuloendothelial system (RES) organ, liver, did not change with variations of the anti-ICAM surface density. In fact, the hepatic uptake of any anti-ICAM/particle formulation was not different from that of IgG/particles. The same result, i.e., lack of significant difference in the uptake of various particle formulations, has been observed in the second main RES organ, spleen. Further, cardiac uptake of the particles, reflecting nonspecific uptake in the tissues other than RES, was the same for all particles regardless of the number of anti-ICAM molecules (Fig. S8). This data indicate that only uptake in the pulmonary vasculature is dependent on the number of anti-ICAM molecules, thus the model does not have to account for nontargeted tissues.

S9. Comparison with AFM Measurements. ***AFM theory.*** From the Bell model, the dissociation rate $k(f)$ of a bound complex under a pulling force f can be calculated as $k(f) = k^0 \exp(f\gamma/k_BT)$, where k_B is the Boltzmann constant and T is the absolute temperature, k^0 is the dissociation rate constant at equilibrium ($f = 0$) and γ represents the distance between the bound state and transition state. Both k^0 and γ are parameters of the Bell model, which as discussed in the following, may be evaluated from the PMF profiles between the NC and the EC surface. Under the pulling force f, the probability distribution of the rupture force is given by:

$$P(f) = k^0 \exp\left(\frac{\gamma f}{k_BT}\right) \exp\left\{\frac{k^0 k_BT}{\gamma r_f}\left[1 - \exp\left(\frac{\gamma f}{k_BT}\right)\right]\right\}. \qquad [S2]$$

where r_f is the loading rate.

We estimate the equilibrium dissociation constant k^0 from the Transition State Theory (TST),

$$k^0 = \frac{k_BT}{h}\exp\left(\frac{-\Delta G}{k_BT}\right), \qquad [S3]$$

where $h = 6.6 \times 10^{-34}$ Js is the Planck's constant and ΔG is the free energy change from bound state to transition state. From the PMF profile, the free energy change $\Delta G \sim 32k_BT$ at temperature

$T = 300$ K. Substitution of the above parameters yields $k^0 \sim 0.08$ s^{-1}. We estimate γ as the distance between equilibrium position and the position of the transition state for the first bond to rupture, and this yields $\gamma \sim 0.2$ nm from the PMF profile; this value is in quantitative agreement with reactive compliance values reported in single molecule force spectroscopy experiments (5, 12). Using the estimated values of k^0 and γ and Eq. **S2**, we plot the distribution of the rupture (unbinding) force distribution at different loading rates in Fig. 5 of the main manuscript. A sensitivity analysis reveals that in Eq. **S2**, the value of the mean rupture force is much more sensitive to γ than k^0. For a fixed loading rate of 10,000 pN/s, we varied γ and k^0 and computed the mean rupture force: for $\gamma = 0.2$ nm and $k^0 = 0.08$ s^{-1}, the mean rupture force is 168 pN. Changing $\gamma = 0.4$ nm (increase by 100%) and holding $k^0 = 0.08$ s^{-1} changes the mean rupture force to 91 pN. In the other limit, holding γ constant at 0.2 nm and changing k^0 to 0.16 s^{-1} (increase by 100%), changes the mean rupture force to 154 pN. Noting that γ is governed by the nature of the antibody-antigen interaction, but the size of the NC impacts k^0 rather than γ, our model predicts that the rupture force distribution is rather insensitive to the size of the NC. Indeed, the mean rupture force in Fig. 4 is very close to that in Fig. S9 (see below).

AFM experiment. Atomic force microscopy allows observation of binding interactions at the molecular level. In particular, it enables measurement of the rupture force between an adhesive pair by generating force-distance curves as one member of the adhesive pair on the AFM cantilever is repeatedly approached and withdrawn from its binding partner immobilized on the probed surface (13, 14). This technique is utilized to experimentally quantify the rupture force between a surface coated with ICAM-1 and anti-ICAM antibody-coated NCs (7).

An AFM force displacement trace is provided in Fig. S9*A* showing triplet rupture events. In Fig. S9*B*, we report the rupture force distribution ICAM-1 surface and AFM tip functionalized directly with antibodies; the mean rupture force is 291 pN and standard deviation is 32 pN over 174 experiments. These values for the rupture of anti-ICAM-1 molecules directly functionalized on the AFM tip are in close agreement with the values when the AFM tips are functionalized with the NCs.

1. Agrawal NJ, Radhakrishnan R (2007) Role of glycocalyx in mediating nanocarrier cell adhesion explored using a thermodynamic model and Monte Carlo simulation. *J Phys Chem C* 111: 15848 –15856.
2. Muro S et al. (2006) Endothelial targeting of high-affinity multivalent polymer nanocarriers directed tointercellular adhesion molecule 1. *J Pharmacol Exp Ther* 317: 1161–1169.
3. Kirchhausen T, Staunton DE, Springer TA (1993) Location of the domains of ICAM-1 by immunolabeling and single-molecule electron microscopy. *J Leukocyte Biol* 53: 342–346.
4. Berman HM et al. (2000) The protein data bank. *Nucl Acids Res* 28: 235–242.
5. Zhang X, Wojcikiewicz E, Moy VT (2002) Force spectroscopy of the leukocyte function-associated antigen-1/intercellular adhesion molecule-1 interaction. *Biophys J* 83: 2270 –2279.
6. Weinbaum S, Zhang X, Han Y, Vink H, Cowin C (2003) Mechanotransduction and flow across the endothelial glycocalyx. *Proc Natl Acad Sci USA* 100: 7988–7995.
7. Calderon AJ, Muzykantov V, Muro S, Eckmann DM (2009) Flow dynamics, binding and detachment of spherical carriers targeted to ICAM-1 on endothelial cells. *Biorheology* 46: 323–341.
8. Squire JM et al. (2001) Quasi-periodic substructure in the microvessel endothelial glycocalyx: A possible explanation for molecular filtering. *J Struct Biol* 136: 239–255.
9. Mulivor AW, Lipowsky HH (2002) Role of glycocalyx in leukocyte-endothelial cell adhesion. *Am J Physiol-Heart C* 283: H1282-H1291.
10. Carlsson J, Åqvist J (2005) Absolute and relative entropies from computer simulation with applications to ligand binding. *J Phys Chem B* 109: 6448–6456.
11. Dill K, Bromberg S (2002) in *Molecular Driving Forces: Statistical Thermodynamics in Chemistry and Biology*, (Taylor & Francis, New York), pp 519–521.
12. Hanley W et al. (2003) Single molecule characterization of P-selectin/ligand binding. *J Biol Chem* 278: 10556–10561.
13. Florin EL, Moy VT, Gaub HE (1994) Adhesion forces between individual ligand-receptor pairs. *Science* 264: 415 –417.
14. Dufrene YF, Hinterdorfer P (2008) Recent progress in AFM molecular recognition studies. *Pflug Arch Eur J Phy* 256: 237–245.

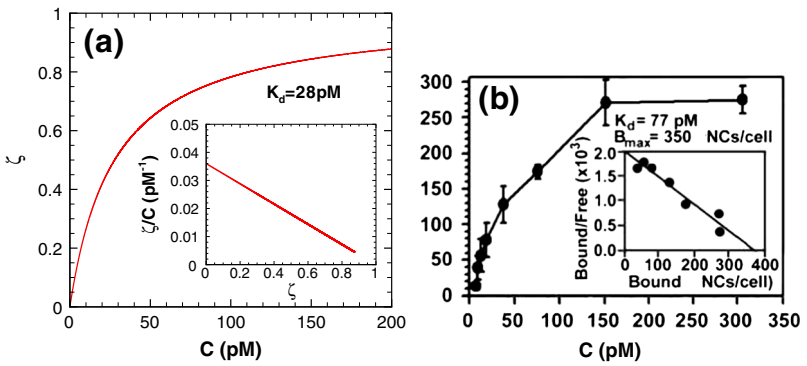

Fig. S1. Calculated fractional binding as function of NC concentration (*a*) compared with experimental measurement from (2) (*b*).

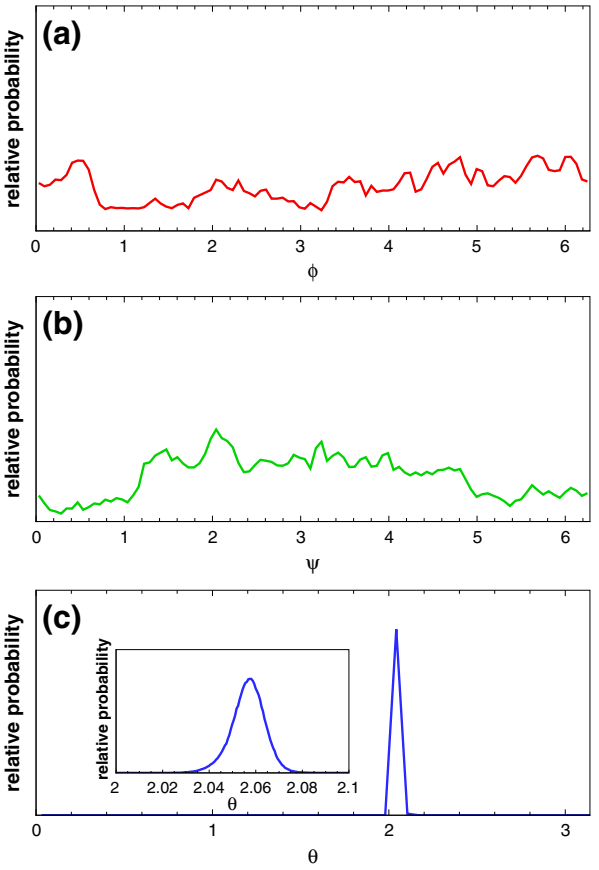

Fig. S2. The distributions of three Euler angles in bound state based on which the rotational volumes are computed. The distribution of ϕ (*a*) and ψ (*b*) are uniform, and the distribution of θ is Gaussian centered around a specific angle (*c*). The Euler angles are expressed in units of radians.

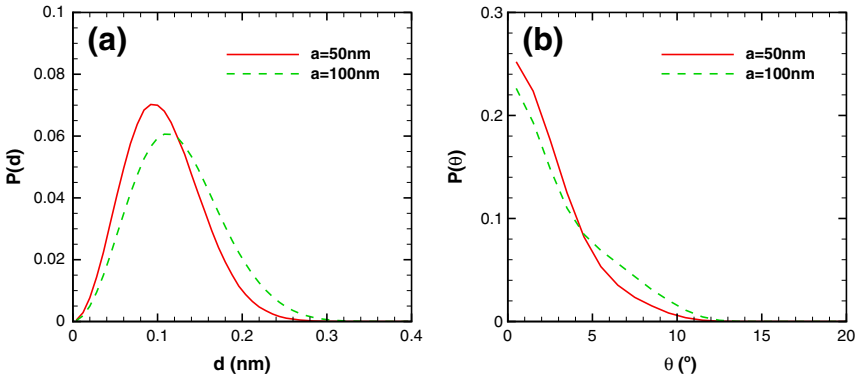

Fig. S3. The distribution of the reaction bond length *d* (*a*) and ICAM-1 bending angle θ (*b*) at equilibrium position for NCs with radius of 50 nm (red solid lines) and 100 nm (green dashed lines).

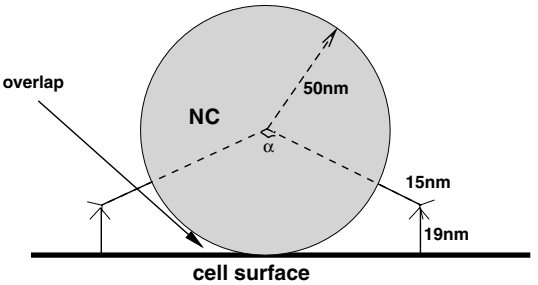

Fig. S4. The schematic on how to estimate the antibody surface coverage at which the multivalency changes from 2 to 1.

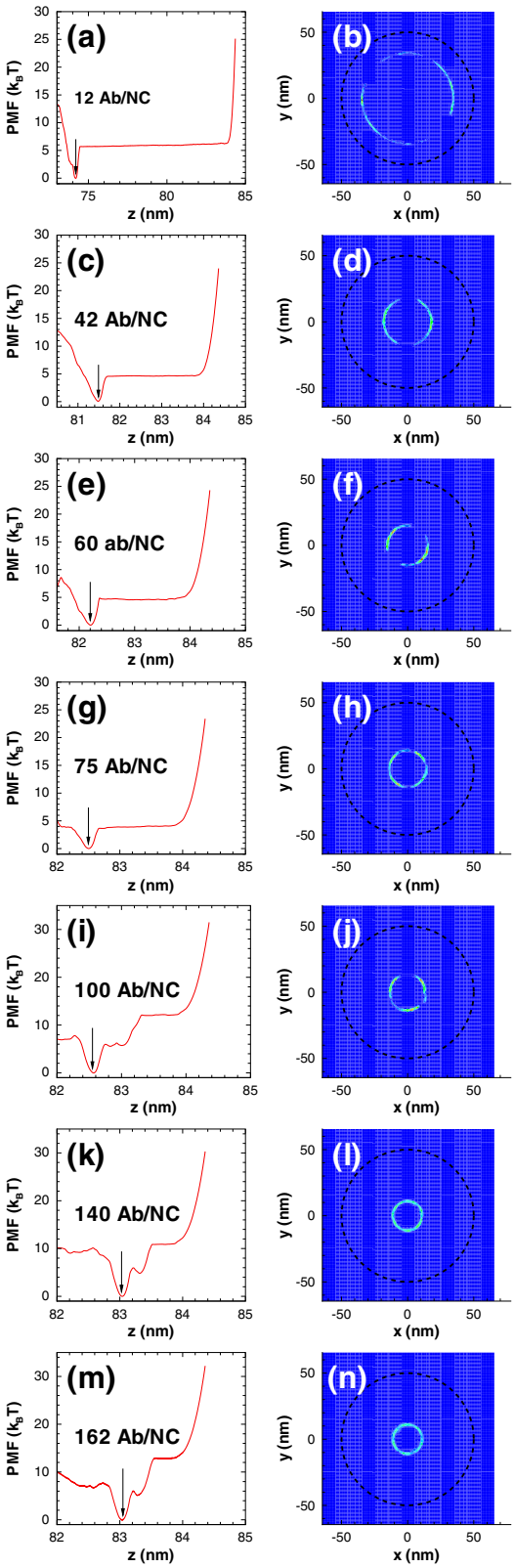

Fig. S5. The PMF profiles and the corresponding bond distributions at different antibody surface coverages σ_s. Each figure corresponds to a data point in Fig. 3*A* of the main manuscript. The dotted lines indicate the boundary of the NC as defined in Fig. 2*B* in the main manuscript.

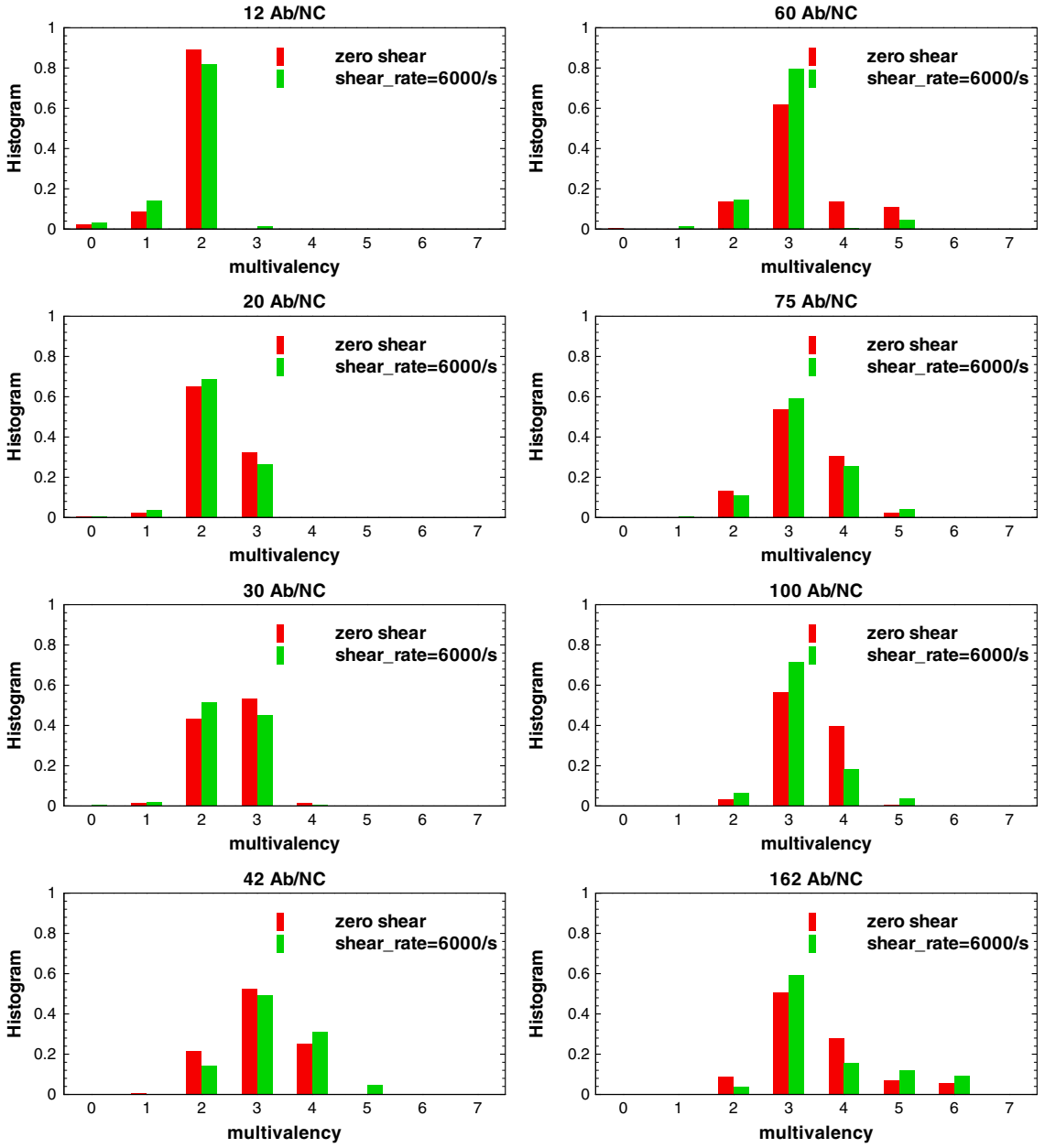

Fig. S6. The histogram of multivalency at different antibody surface coverages with/without shear flow (shear stress of 6 Pa). As shown, the shear stress produces evident effect only at small antibody surface coverages ≤30 Ab/NC in good agreement with *in vitro* experiments using 1 μm particles (see figure 5 in ref. 7).

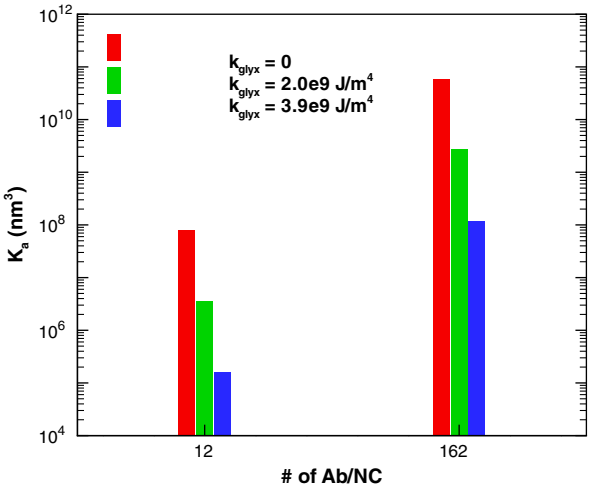

Fig. S7. The effect of glycocalyx on binding affinities for the smallest and largest antibody surface coverage σ_s at two different glycocalyx stiffness k_{glyx}. The glycocalyx effectively reduces the binding affinities by a constant value for all antibody surface coverages.

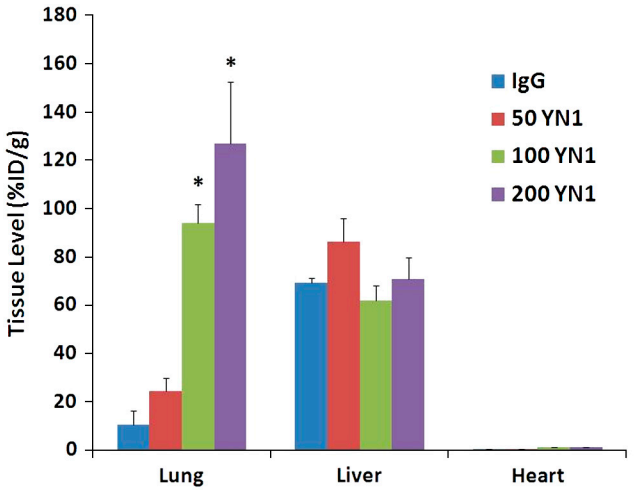

Fig. S8. Tissue level (percent of injected dose per gram of tissue), was determined in naive mice 30 minutes post-injection for NCs with varying surface coverage of anti-ICAM-1 molecules. Organs presented here include lung, liver, and heart as representative organs of targeted tissue, reticuloendothelial system (RES) tissue, and nonspecific tissue. "*" denotes statistical significance between experimental groups and IgG control, $p < 0.05$.

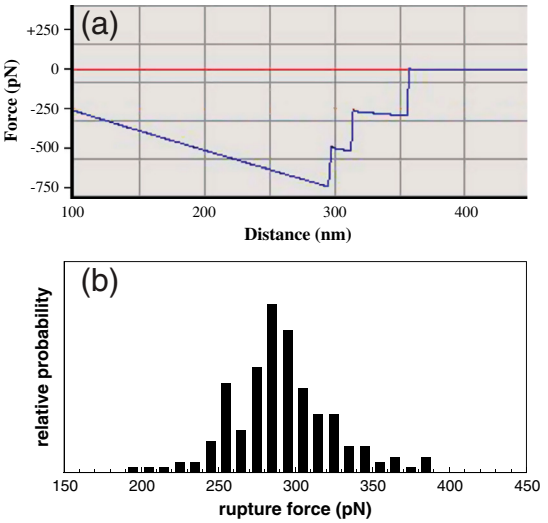

Fig. S9. (*a*) AFM trace showing multiple rupture events obtained using a time-sampling of 2,000 s^{-1}. (*b*) The rupture force distribution of the interaction between ICAM-1 and anti-ICAM-1 obtained in AFM experiments using a time sampling of 12,000 s^{-1}.

Table S1. Parameters used in the model

parameter	value	ref
simulation surface area	1 μm^2	(1)
simulation height	0.5 μm^2	(1)
nanocarrier diameter	100 nm	(2)
antigen length	19 nm	(3)
antibody length	15 nm	(4)
number of antigens	2000	(2)
number of antibodies per nanocarrier	from 12 to 162 (5 to 74% of saturation coverage)	(2)
free energy change at equilibrium per bond, ΔG_0	-7.98×10^{-20} J	(2)
bond spring constant, k	1,000 dyn/cm	(5)
antigen flexural rigidity	7,000 pN·nm^2	(6)
flow shear rate, S	6,000 s^{-1}	(7)
glycocalyx height, h	100 nm	(8)
glycacalyx stiffness, k_{glyx}	3.9×10^9 J/m^4	(9)
system temperature	27 °C	